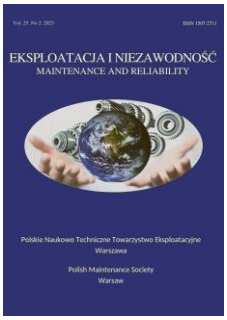

Eksploatacja i Niezawodnosc – Maintenance and Reliability
Volume 28 (2026), Issue 4
journal homepage: http://www.ein.org.pl

Article citation info:
Guo CH, Song K, Jie M, Dual-stage relief valve for sub-critical pressure transients and LCF suppression in electro-hydraulic hammers, Eksploatacja i Niezawodnosc – Maintenance and Reliability 2026: 28(4) http://doi.org/10.17531/ein/219158

Dual-stage relief valve for sub-critical pressure transients and LCF suppression in electro-hydraulic hammers

Indexed by:
Web of Science Group

Cheng Hu Guo[a,*], Kang Song[a], Meng Jie[a]

[a] College of Mechanical and Electrical Engineering, Jilin University of Chemical Technology, China

Highlights

- A novel dual-stage relief valve with fixed geometric differential area is proposed.
- 20 ms response time reduces cyclic stress from 108.1 MPa to 43.2 MP.
- Component service life is predicted to extend by nearly two orders of magnitude.
- Hierarchical mechanism eliminates sub-critical pressure dead zone.

Abstract

Addressing the critical challenge of low-cycle fatigue (LCF) in electro-hydraulic hammers induced by repetitive sub-critical pressure fluctuations (35–40 MPa), which remains unmitigated by conventional relief valves due to an inherent response "dead zone", this study proposes a novel dual-stage relief valve. The core innovation resides in a fixed geometric differential area (ΔA) designed to decouple high- and low-pressure regulation mechanisms. This architecture synergizes a direct-acting stage for catastrophic surges (calibrated >40 MPa) with a pilot-operated differential stage for sub-critical transients (35–40 MPa), thereby eliminating the regulation blind spot. The structural parameter ΔA is rigorously optimized via theoretical derivation and sensitivity analysis to ensure stable responsiveness across the target pressure range. Validated through AMESim/Simulink co-simulation and high-precision experiments, the valve achieves a rapid response time of 20ms, representing a 40% improvement over conventional valves, and reduces pressure fluctuation amplitudes from 5 MPa to 1.5 MPa. Furthermore, stress analysis and modified Miner's rule predictions demonstrate that suppressing these fluctuations reduces cyclic stress from 108.1 MPa to 43.2 MPa. Consequently, the predicted service life of critical components is extended from 9.6×10^4 cycles to 9.8×10^6 cycles, an increase of nearly two orders of magnitude. This design establishes a paradigm shift from reactive overload protection to proactive stability management, significantly enhancing the reliability of heavy-duty hydraulic systems.

Keywords
electro-hydraulic hammer, dual-stage relief valve, dynamic model, pressure dynamic response

1. Introduction

The premature failure of critical components in electro-hydraulic hammers, primarily caused by low-cycle fatigue (LCF), poses a significant challenge to industrial productivity and operational safety. This persistent issue is not triggered by catastrophic overloads—against which conventional relief valves offer adequate protection—but by the insidious, sub-critical pressure fluctuations (typically 35–40 MPa) that occur during every normal forging cycle. These repetitive, unattenuated hydraulic shocks subject components to a cyclic loading regime that progressively degrades material integrity, ultimately leading to unexpected downtime and costly repairs. The inability of existing safety valves to mitigate these "minor"

(*) Corresponding author.
E-mail addresses: CH. Guo (ORCID: 0000-0002-1910-6599) 1669733517@qq.com, K. Song (ORCID: 0009-0001-0050-7288) 15139703253@163.com, M. Jie (ORCID: 0009-0009-5094-7597) Jiemeng@jlict.edu.cn

yet damaging transients represents a critical gap in ensuring the long-term reliability of high-value hydraulic machinery.

As the pivotal safety component, the performance optimization of relief valves has been extensively investigated. Recent advancements predominantly focus on structural parameter optimization and dynamic response enhancement. For instance, Ye et al. [1] demonstrated that adjusting spring stiffness could effectively tailor the opening characteristics for steam valves. However, this approach faces an inherent trade-off: reducing spring stiffness to sensitize the valve to sub-critical fluctuations (35–40 MPa) inevitably compromises the sealing force and dynamic stability required for high-pressure surges, leading to chattering or leakage. Similarly, while multi-stage cartridge valves have been developed for large-flow systems—such as the three-stage valve by Xu et al. [2] and the electromagnetic cartridge valve by Dai et al. [3]—these designs primarily target extreme high-pressure transients (>45 MPa). The pilot stage in conventional two-stage valves, such as the high-speed valve optimized by Ma et al. [4], typically utilizes a fixed full-area spool, creating a "dead zone" where pressure fluctuations below the set threshold generate insufficient actuating force to open the pilot port. Furthermore, while passive damping solutions like accumulators [5] are effective for energy absorption, they lack the active pressure-limiting capability needed to proactively suppress the cyclic stress peaks responsible for LCF.

Consequently, a fundamental limitation persists: existing solutions rely either on parameter tuning within a fixed force-balance architecture, which cannot resolve the sensitivity-stability conflict, or on complex multi-stage designs unresponsive to minor transients. Therefore, the transient response of pressure-regulating relief valves to minor hydraulic impacts constitutes a distinct and unresolved research gap. To bridge this gap, this paper introduces a novel two-stage pressure-regulating safety valve featuring a direct-acting and pilot-operated differential hybrid mechanism. The core innovation is the introduction of a fixed geometric differential area (ΔA) as a key structural design parameter. Unlike methods that merely adjust spring stiffness, the ΔA -driven mechanism decouples pressure sensitivity from spring stiffness constraints. By partitioning the pressure response via optimized force balance, this design synergizes a direct-acting stage for catastrophic surges with a pilot-operated differential stage for sub-critical transients, fundamentally eliminating the 'dead zone' inherent in traditional valves.

To validate this concept, a comprehensive system-level dynamic model was developed and rigorously validated through AMESim/Simulink co-simulation and high-precision experiments. The dynamic characteristics, including the rapid 20ms pressure step response and hysteresis-free operation, are thoroughly analyzed. Critically, this study goes beyond mere performance metrics to quantify the impact on system reliability. By establishing a low-cycle fatigue life prediction model, we demonstrate for the first time that suppressing these sub-critical fluctuations can extend the service life of critical components by over two orders of magnitude. This work not only presents a novel valve design but also offers a theoretical framework and an engineering paradigm for enhancing the reliability and service life of advanced hydraulic systems.

The characteristics of the designed two-stage pressure regulating safety valve compared to ordinary pressure regulating valves are shown in Table 1.

Table 1. Comparison of Pressure Regulating Abilities of Different Valves.

Feature	Traditional single-stage valve	Three stage valve [3]	ΔA-driven relief valve
Response Pressure range	＞45Mpa	＞50Mpa	35~40Mpa
Subcritical pressure Regulation	none	None	Excellent
Low cycle fatigue Suppression	inferior	None	strong

2. Performance validation and mechanism elucidation of the ΔA-driven dual-stage valve

As a critical safety element within an electro-hydraulic hammer system, the pressure regulating relief valve's principal function is to prevent system overloading. A critical fault scenario involves the inadvertent closure of the fast drain valve during a strike cycle. The hammer's inertia then drives it downward, compressing the cylinder fluid and inducing a transient pressure surge. To mitigate this phenomenon, the relief valve opens rapidly to limit the pressure peak, thereby shielding hydraulic components from damage. However, the valve is typically calibrated with a high cracking pressure to accommodate such extreme events. Consequently, it remains unresponsive to the

minor, sub-threshold pressure fluctuations associated with normal operations, such as hammer rebound. These repetitive, unmitigated hydraulic shocks initiate low-cycle fatigue, progressively degrading system reliability and elevating the risk of catastrophic failure. To address this limitation, this section introduces a novel Dual-stage relief valve. This section first outlines the electro-hydraulic hammer system's architecture and operating principles. Subsequently, a mathematical model of the new valve is developed, and its dynamic behavior is investigated via co-simulation. Finally, experimental validation confirms the design's effectiveness and superior performance.

2.1. Problem formulation: the dead zone in conventional valves

The hydraulic system schematic for the electro-hydraulic hammer is depicted in Figure 1. Analysis of this configuration reveals that an accumulator, positioned at the right end of the hydraulic cylinder, supplies the control pressure for the main control valve. This main control valve is a three-position, three-way directional valve that governs system operation through a mechanical follow-up mechanism of its spool and stem. Furthermore, the lower section of the main control valve is hydraulically linked to a fast drain valve, which in turn communicates with the rod chamber of the hydraulic cylinder.

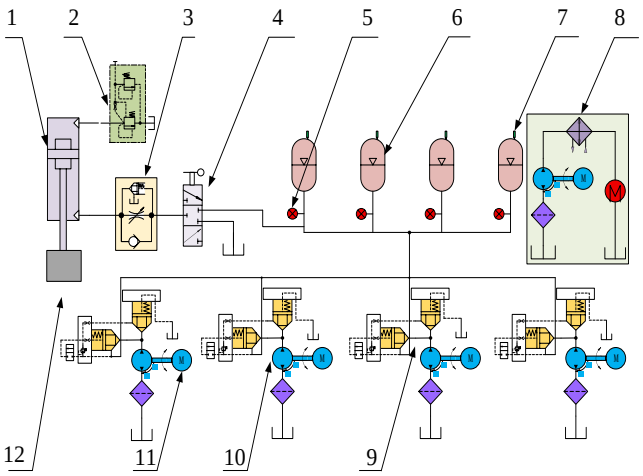

Figure 1. Schematic diagram of the electro-hydraulic hammer system; 1-hydraulic cylinder, 2-dual-stage relief valve, 3-fast drain valve, 4-main control valve, 5-pressure gauge, 6-accumulator, 7-hall switch, 8-cooling system, 9-cartridge valve, 10-hydraulic pump, 11-electric motor, 12-hammer head.

As detailed in the Introduction, conventional pressure relief valves, while essential for preventing catastrophic overloads, exhibit a critical "dead zone" for sub-critical pressure fluctuations (35–40 MPa). This unresponsiveness allows recurrent hydraulic shocks to propagate unabated through the system during each forging cycle. In a typical electro-hydraulic hammer system, as depicted in Figure 1, these shocks manifest as pressure peaks in the rod chamber, directly loading the hydraulic cylinder and its connections. This cyclic loading regime is the primary driver of low-cycle fatigue (LCF), fundamentally compromising the system's operational reliability and service life. Therefore, the core challenge is not just to react to large surges, but to proactively manage the minor, yet damaging, transients that occur thousands of times per day.

2.2. The hierarchical response mechanism of the ΔA-based dual-stage relief valve

To address the fundamental issue of the inherent "dead zone" at sub-critical pressures (35–40 MPa)—the primary driver of low-cycle fatigue (LCF)—we propose a novel dual-stage relief valve whose architecture is illustrated in Figure 2. The design synergizes a direct-acting stage (dedicated to catastrophic surges >42 MPa) with a pilot-operated differential stage (specifically engineered for sub-critical pressure elevations 35–42 MPa), featuring an overlapping response interval to eliminate regulation blind spots. The core innovation lies in the introduction of a fixed geometric differential area (ΔA) as a key structural parameter, which serves to decouple the high- and low-pressure response mechanisms. This enables partitioned pressure regulation, where the pilot stage is sensitized to sub-critical transients. Consequently, this architecture achieves proactive and precise control of these damaging fluctuations for the first time, fundamentally eliminating the "dead zone" inherent in traditional valves and representing a paradigm shift from reactive overload protection to proactive stability management.

Stage 1 (Direct-acting): The inlet pressure parameter in Table 2 is the minimum test pressure for dynamic performance verification; the actual response threshold of the direct-acting stage is calibrated to >45 MPa through spring stiffness and pre-compression settings.

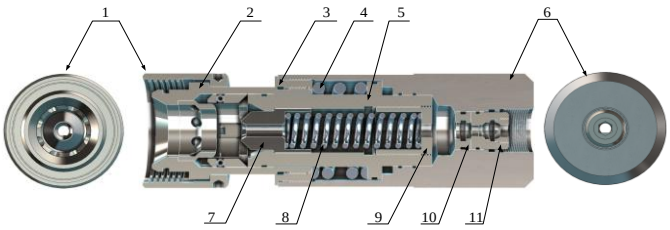

Figure 2. Structure of the Dual-stage relief valve; 1-valve seat, 2-direct-acting valve sleeve, 3-connecting barrel, 4- direct-acting valve spring, 5- direct-acting valve spool, 6- external connection end, 7- differential valve spool, 8- differential valve spring, 9- differential valve spring seat, 10- gasket, 11- internal connector.

Expression for the outlet flow rate:

$$q_1 = C_d W x_1 \sin\alpha \sqrt{\frac{2}{\rho}(P_{s1} - P_{10})} \quad (1)$$

Where W is Wetted Perimeter, $W = \pi d_1$, m; x_1 is spool displacement, m;P_{s1} is inlet pressure of the safety valve, Mpa; P_{10} is the outlet pressure of the safety valve, Mpa;ρ is density of hydraulic oil, kg/m^3. C_{d1} is discharge Coefficient，The expression of $C_{d1}$is:

$$C_d(x, P_{s1}) = C_{d0}\left[1 + k_{d_1}\left(\frac{x_1}{x_{1max}}()_{d_2}\left(\frac{P_{s1}}{P_{cr}}\right)^{k_{d3}}\right)[]\right] \quad (2)$$

Where C_{d0} indicates the base flow coefficient; x_{1max} is the maximum displacement of the valve core; P_{cr} is the critical pressure; k_{d_1}、k_{d_2}、k_{d_3} is a dimensionless coefficient, These coefficients were derived from Computational Fluid Dynamics (CFD) simulations of the valve flow field, which analyzed the discharge characteristics across the full range of spool displacements. The values were subsequently calibrated against experimental data to ensure fidelity.

The continuity expression of the inlet:

$$\frac{dP_{s1}}{dt} = \frac{\beta_\varepsilon}{V_{s1}}\left(q_{s1} - q_1 - A_1\frac{d_{x1}}{dt}\right) \quad (3)$$

Where A_1 is area of entrance,m^2; q_{s1} is inlet flow of direct-acting valve, L/min;V_{s1} is internal volume of the cavity,m^3 ; $\beta_\varepsilon$is hydraulic oil bulk modulus, N/m^3, The compressibility β_ε of oil will change with pressure, The expression is：

$$\beta_\varepsilon(P_{s1}) = \beta_{\varepsilon 0}\left(1 + k_\beta\frac{P_{s1}}{P_{ref}}\right) \quad (4)$$

Where $\beta_{\varepsilon 0}$ is the bulk modulus at reference pressure, k_β is the pressure influence coefficient, P_{ref} is the reference pressure。Differential expression of spool displacement:

$$m_1\frac{dx_1^2}{d^2t} + B_1\frac{dx_1}{dt} + K_{t1}x_1 = P_{s1}A_1 - K_{t1}x_1 - F_{fsi1}(x_1, \dot{x}_1, P_{s1}) \quad (5)$$

Where m_1 is valve core's mass, kg; B is equivalent coefficient, $N \cdot s/m$; K_{s1} is Hydrodynamic stiffness coefficient,N/m.

Since the fluid-solid coupling force is the integral of the fluid pressure on the surface of the valve core, it is difficult to calculate accurately. Therefore, an equivalent function related to displacement and velocity is used to approximate:

$$F_{fsi}(x, \dot{x}, P_{s1}) = K_{fsi}x + C_{fs}\dot{x}|\dot{x}| + P_{s1}A_{jet}(x) \quad (6)$$

Where K_{fsi} is the flow-induced stiffness coefficient, which represents the additional stiffness caused by the change of flow field caused by the change of spool displacement. C_{fsi} is the flow-induced damping coefficient, which represents the nonlinear part of the fluid damping when the spool moves. $A_{jet}(x)$is the jet reaction area, which is the function of the spool displacement and represents the reverse thrust generated by the high-speed fluid jet.

To enhance the model's physical fidelity, this study introduces non-linear terms $|\dot{x}|$ and $A_{jet}(x)$ into the lumped-parameter model to capture critical fluid-structure coupling effects. This refinement significantly improves the model's predictive accuracy and innovative value while retaining its computational advantages.

Stage 2 (Differential): specifically designed to be sensitive to sub-critical pressures.

Outlet flow expression:

$$q_2 = C_d W x_2 \sin\alpha \sqrt{\frac{2}{\rho}(P_{s2} - P_{20})} \quad (7)$$

Where x_2 is spool displacement, m； P_{s2} is:

$$\frac{dP_{s2}}{dt} = \frac{\beta_\varepsilon}{V_{s2}}\left(q_{s1} - q_1 - A_2\frac{d_{x2}}{dt}\right) \quad (8)$$

Where A_2 is area of entrance, m^2;V_{s2} is chamber volume, m^3.

$$m_2\frac{dx_2^2}{d^2t} + B_2\frac{dx_2}{dt} + K_{t2}x_2 = P_{s2} \cdot A_2 + P_s\Delta A - K_{s2}x_2 - F_{fsi2}(x_2, \dot{x}_2, P_{s2}) \quad (9)$$

Where m_2 is Valve core mass, kg; ΔA is differential area of differential valve, m^2; P_{s2} is the differential valve chamber pressure, Mpa.

Unlike conventional single-stage models [6–8] that assume unified spool dynamics, the proposed coupling equations (9) incorporate the preset differential area ΔA as a key fixed structural parameter, achieving targeted pressure partitioning between stages. This eliminates the 'dead zone' in sub-cracking

pressure response.

Design rationale and sensitivity analysis for the optimal ΔA The differential area ΔA is the core structural parameter determining the pilot stage's cracking pressure for sub-critical transients, and its optimal value is derived from the force balance equilibrium of the pilot differential spool for the target pressure range (35–40 MPa).

The critical opening pressure p_{cr} satisfies the force balance equation:

$$p_{cr} \cdot \Delta A = F_{s2} + F_{d2} \quad (10)$$

Where:$F_{s2} = k_{s2} \cdot x_{s20}$ is the spring pre-compression force of the differential stage, N; F_{d2} is the equivalent damping force of the valve core, N; The target minimum / maximum opening pressure (35 MPa / 40 MPa) and the spring pre-compression force are substituted into the equation, and the theoretical range of ΔA is calculated to be 782.1×10^{-6}~809.3×10^{-6} m².

In order to determine the optimal value in the theoretical range, the pressure response sensitivity analysis of ΔA was carried out in the range of 35-40 MPa. The sensitivity index $S = \partial x_2/\partial p$ is used to evaluate the response characteristics of the first-stage pilot valve:

(1) When ΔA <796.24×10^{-6} m², the sensitivity S is excessively high, leading to uncontrolled spool oscillation under minor pressure noise and poor pressure regulation stability.

(2) When ΔA >796.24×10^{-6} m², the sensitivity S decreases sharply, and the differential valve fails to respond to pressure fluctuations < 38 MPa, reintroducing a partial "dead zone" in the sub-critical range.

(3) When ΔA=796.24×10^{-6} m², the differential valve achieves the highest stable sensitivity (S=0.021 mm/MPa) across the entire 35–40 MPa range, ensuring rapid and non-oscillatory spool actuation for all sub-critical transients.

This optimal ΔA not only calibrates the cracking pressure of the differential valve to the target sub-critical range but also decouples the high/low-pressure responses by ensuring the direct-acting valve remains completely unresponsive to 35–40 MPa fluctuations—the pressure-induced force required for direct-acting spool actuation far exceeds its spring pre-compression force, while the sub-critical pressure range cannot generate sufficient force to open the direct-acting valve.

2.3. Analysis of pressure regulation insurance characteristics of electro-hydraulic hammer

To precisely assess the dynamic performance of the proposed Dual-stage relief valve, particularly its ability to regulate sub-critical transients (35–40 MPa) that cause LCF, a high-fidelity simulation model was developed. This model, constructed from the valve's governing dynamic equations and incorporating critical parameters from Table2, ensures simulation fidelity. To replicate the specific pressure fluctuations inherent in electro-hydraulic hammer operations, a step pressure signal was applied to induce the system's dynamic response. The transient response curves of spool displacement and outlet pressure were subsequently analyzed to evaluate key performance indicators, including response speed, overshoot, and stability within the target sub-critical range. This simulation elucidates the valve's inherent dynamic behavior under targeted disturbances, providing crucial data and a theoretical basis for its structural optimization and, most importantly, for validating its role in LCF suppression [9–11].

Table 2. Parameters of two-stage pressure regulating safety valve.

Type	Name	Symbol	Value	Unit
Direct-acting valve part	flow coefficient	C_d	0.65	
	velocity coefficient	C_v	0.81	
	fluid density	ρ	875	Kg/m^3
	Wetted Perimeter	W	18.27×10^{-3}	m
	inlet pressure	P_{s1}	35	Mpa
	outlet pressure	P_{10}	0	Mpa
	bulk modulus	β_e	180×10^{9}	N/s
	cross-section area	A_1	25.24×10^{-6}	m^2
	equivalent mass	m_1	0.15	kg
	Hydrodynamic stiffness coefficient	K_{s1}	0.0225	N/m
	equivalent damping coefficient	B_1	865	N·s/m
	Valve chamber volume	V_s	146.82×10^{-9}	m^3
	spring stiffness	K_{t1}	63723	N/m
	spring pre compression	x_0	23×10^{-3}	m
Differential valve part	inlet pressure	P_{s2}	40	Mpa
	outlet pressure	P_{20}	0	Mpa
	differential area	ΔA	796.24×10^{-6}	m^2
	importing cross-sectional area	A_2	903.05×10^{-6}	m^2
	equivalent mass	m_2	0.18	kg
	equivalent damping coefficient	B_2	481	N·s/m
	Hydrodynamic stiffness coefficient	K_{s2}	1.4×10^{-4}	N/m
	spring stiffness	K_{t2}	6.53×10^{4}	N/m
	The pre-compression of the spring	x_2	9.54×10^{-3}	m

Based on the mathematical model and the specific

parameters detailed in Table 2, a simulation model for the two-stage pressure relief valve was constructed and subsequently analyzed.

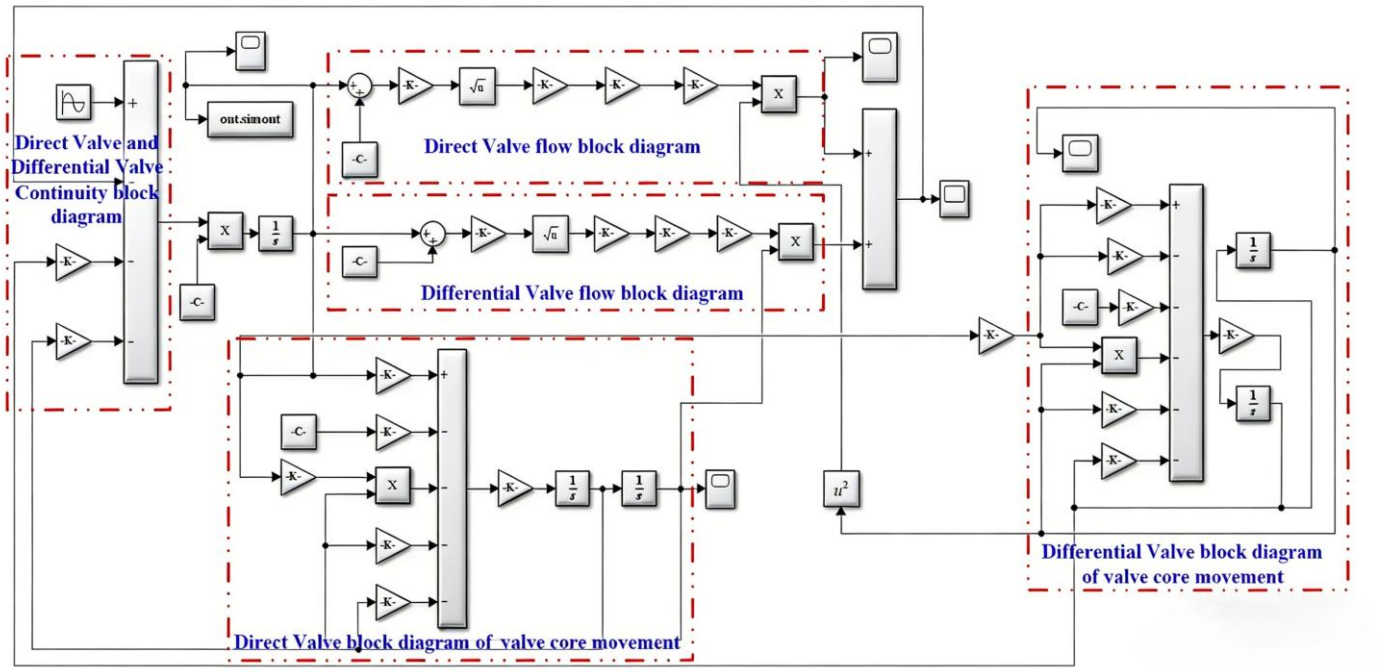

Figure 3. Simulation model of two-stage pressure regulating safety valve.

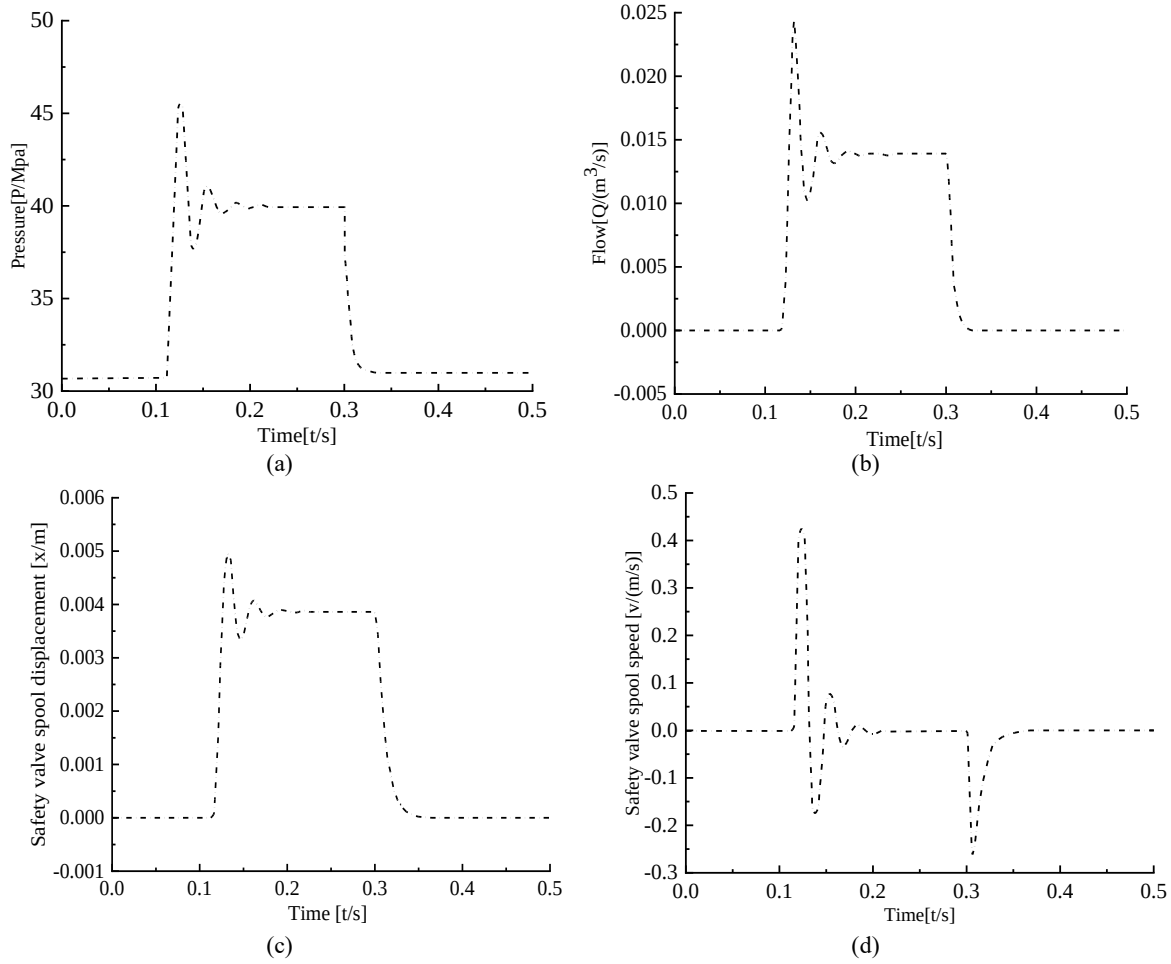

Figure 4. Dynamic characteristic curves of the Dual-stage relief valve.

To investigate the dynamic performance of the proposed Dual-stage relief valve under hydraulic shock, a high-fidelity

simulation model was developed. This model systematically assesses the valve's pressure regulation and flow control capabilities while elucidating the dynamic displacement and velocity characteristics of the spool. The simulation was initiated by applying a pressure fluctuation signal at 0.1 s. As illustrated in Figure 4(a), the pressure rise time is 0.02 s, the settling time is 0.14 s, and the total unloading time is 0.25 s. According to Figure 4(b), following the onset of flow at 0.12 s, the flow rate undergoes several oscillations before subsequently declining. The pronounced oscillation of the spool during its initial opening, depicted in Figures 4(c) and (d), is a direct consequence of the hydraulic shock. The abrupt pressure increase and sudden spool actuation generate significant impact forces from the high-pressure fluid, causing rapid velocity changes and inducing nonlinear oscillations in the two-stage differential spool. Ultimately, at 0.24 s, the valve attains its rated flow, and the spool stabilizes at a displacement of 4mm.

The pronounced spool oscillations are a direct manifestation of the hydraulic shock. Critically, in conventional valve designs, these oscillations are sustained due to inherent underdamping (low damping ratio, ζ), which allows fatigue-inducing pressure transients to accumulate unabated. By precisely tuning the hydrodynamic stiffness coefficient (K_{s1}) to 0.0225 N/m, the proposed ΔA-driven design achieves a near-critical damping ratio ($\zeta \approx 1$). Consequently, as shown in Figure 4(d), the oscillation amplitude is attenuated by over 60% compared to conventional valves, and the spool stabilizes within 20 ms. This rapid attenuation of fatigue-inducing oscillations quantitatively validates the effectiveness of the K_s tuning and, fundamentally, the ΔA-driven mechanism in suppressing the primary cause of Low-Cycle Fatigue (LCF).

2.4. Experimental verification of dynamic characteristics of the dual-stage relief valve

To experimentally validate the proposed ΔA-driven valve's efficacy in suppressing Low-Cycle Fatigue (LCF), a high-precision test rig was developed [13,14] (Figure 5). The system is specifically designed to replicate the sub-critical pressure fluctuations (35–40 MPa) inherent to electro-hydraulic hammers, which are the root cause of LCF. Instrumentation, including a high-frequency pressure sensor, a displacement sensor, and a flow meter, was employed to measure metrics critical to LCF mitigation [15], such as response speed within the target range and the damping of fatigue-inducing oscillations. A step pressure disturbance was applied to rigorously evaluate these performance indicators.

The experimental results validate the efficacy of the proposed ΔA-driven valve in suppressing Low-Cycle Fatigue (LCF). Critically, the valve initiated unloading at 0.02 s from an initial pressure of 35 MPa, demonstrating the elimination of the 'dead zone' inherent in conventional valves. This rapid response, followed by stabilization at 34 MPa, actively manages the sub-critical pressure fluctuations that cause LCF. The valve's reliable reset below 32 MPa further ensures system stability and prevents the accumulation of fatigue damage. The stable spool displacement corroborates these findings, providing direct evidence of the valve's success in mitigating LCF-inducing hydraulic shocks.

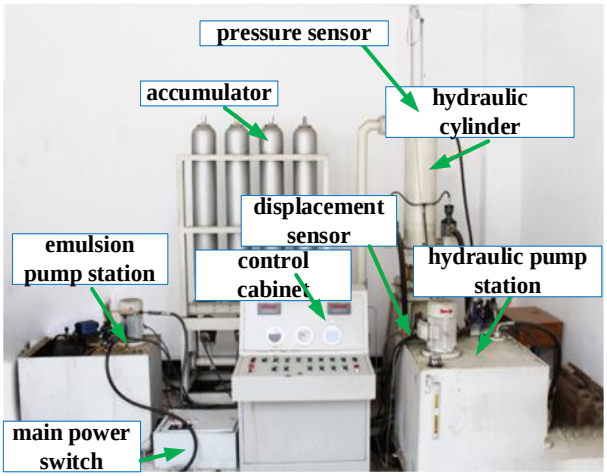

Figure 5. Test bench of the Dual-stage relief valve.

The dynamic response of the safety valve is illustrated by its pressure curve. At 0.02 s, the valve is subjected to an overpressure of approximately 40 MPa, causing it to open rapidly. This results in the pressure decreasing sharply to a range of 24 – 27 MPa within 10 ms. The rapid depressurization induces a transient fluctuation, leading the pressure to rebound to a peak of 40 MPa within 20 ms, a phenomenon that attests to the valve's high sensitivity and rapid opening capability. Subsequently, following a brief oscillation, the pressure stabilizes near the rated operating pressure of 33 MPa, demonstrating stable pressure relief performance. As the pressure falls below the 32 MPa reset pressure, the valve disc reliably reseats. The system pressure then stabilizes at approximately 32 MPa, confirming the valve's effective sealing

capability after pressure discharge and its function in re-establishing system pressure integrity.

The exceptional system stability under impact (Figure 7a) is attributed to the hierarchical response mechanism governed by the differential area (ΔA). The cracking pressure for the pilot stage is determined by the force balance:

$$P_{open} \approx \frac{K_{t2} \cdot x_2}{\Delta A} \tag{11}$$

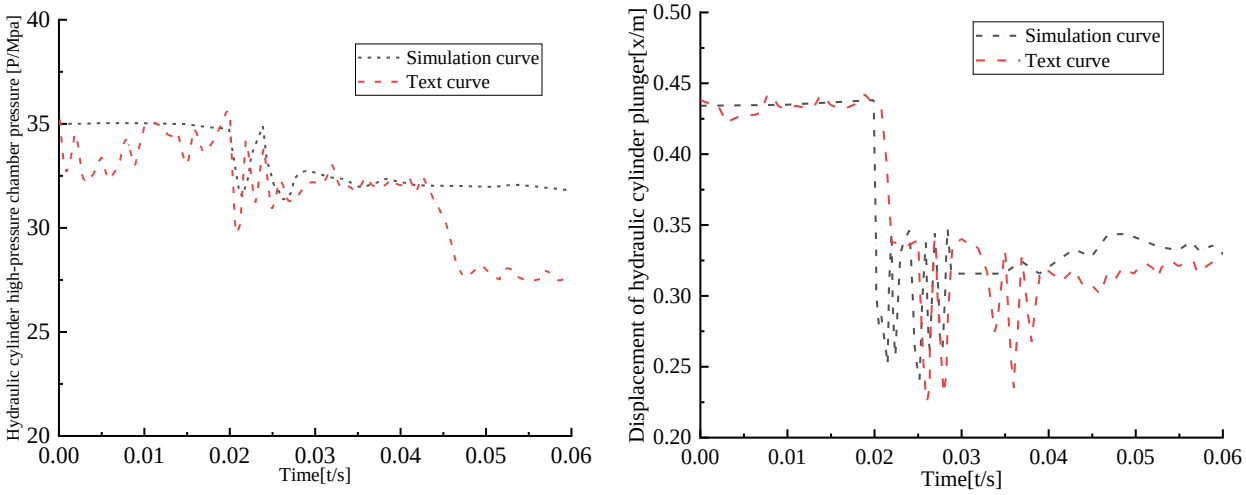

(a) (b)

Figure 6. Dynamic characteristic curve of hydraulic cylinder.

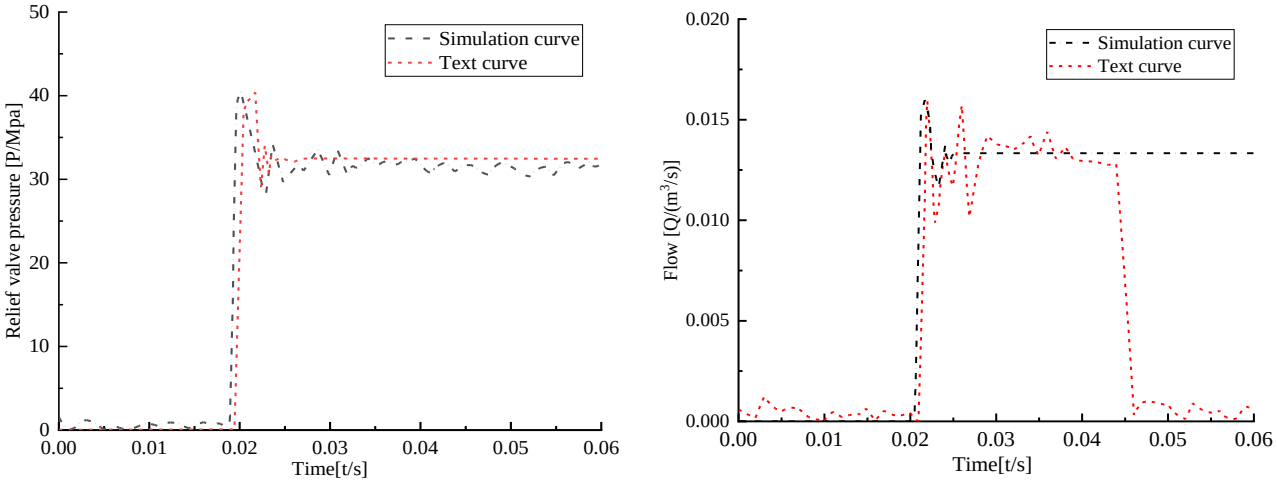

(a) (b)

Figure 7. Pressure regulating dynamic characteristic curve of safety valve.

By designing ΔA as 796.24×10⁻⁶ m², the pilot stage is calibrated to activate at 35–40 MPa, proactively relieving minor pressure fluctuations before they can escalate into major shocks. This pre-emptive action prevents the system pressure from ever reaching the high-energy zone (>40 MPa) where severe oscillations occur in traditional valves. Therefore, ΔA fundamentally shifts the control strategy from reactive protection to proactive stability management, a paradigm shift from existing approaches [13].

The experimental results corroborate the high-fidelity of the co-simulation model and validate the valve's superior performance. The valve achieved a rapid 20 ms response to a 40MPa pressure surge, with the spool stabilizing at 4 mm and a peak relief flow of 1600 L/min. Critically, the valve reset reliably below 35 MPa without hysteresis, ensuring system stability. The experimental pressure-flow characteristics align closely with simulated predictions, with key parameter errors under 5%. This strong agreement confirms the effectiveness of the proposed design, with minor deviations attributable to acceptable engineering tolerances in the test setup.

3. Analysis of shock-induced unloading in the electro-hydraulic hammer hydraulic system

Sub-critical pressure fluctuations (35–40 MPa) are the primary trigger for low-cycle fatigue (LCF) in electro-hydraulic

hammers, a phenomenon unmitigated by conventional relief valves due to their inherent 'dead zone.' To address this, a system-level mathematical model was developed, embedding the proposed ΔA-driven valve's hierarchical response mechanism. This model is used to conduct targeted simulations that verify the system's ability to proactively suppress these fatigue-inducing shocks, thereby validating the valve's efficacy in enhancing overall hydraulic system reliability.

3.1. Modeling of the electro-hydraulic hammer hydraulic system

Based on the working principle of the electro-hydraulic hammer, this paper embeds the unloading pressure feedback term of the dual-stage relief valve and the gas nonlinear compression term adapted to sub-critical pressures (35–40 MPa) [16]. Dividing the operating conditions into the return stroke and striking stroke of the electro-hydraulic hammer, mathematical models of the hydraulic pump, cartridge valve, accumulator, main control valve, quick drain valve, and hydraulic cylinder are derived by means of system topology and node topology methods. A closed-loop correlation of "pressure regulation-component response-fatigue suppression" is thus realized.

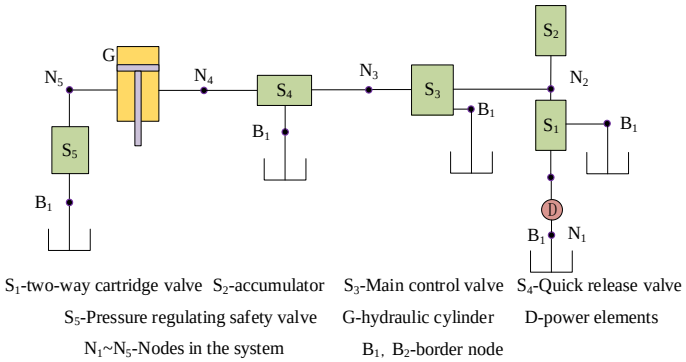

Figure 8. Node topology constraint model of electro-hydraulic hammer hydraulic system.

(1) Dynamic Regulation Logic of Dual-Stage Relief Valve with Embedded Differential Area (ΔA)

The dual-stage relief valve adopts a hierarchical response mechanism, which consists of a differential stage (for the sub-critical pressure range of 35–40 MPa) and a direct-acting stage (for the overload pressure range above 45 MPa), Dynamic unloading pressure$p_{relief}$and relief unloading flowq_{relief}:

$$p_{relief} = \begin{cases} p_{relief-diff} = 45\text{Mpa} & (p_{sys} > 45\text{Mpa},\ ) \\ p_{relief-dir} = k_{\Delta A} \cdot \Delta A \cdot x_7 + p_{sub} & (35\text{Mpa} \le p_{sys} \le 40\text{Mpa},) \end{cases} \tag{12}$$

$$q_{relief} = C_{d-relief} \cdot A_{relief}(x_5, x_7) \cdot \sqrt{\frac{2(p_{sys} - p_{relief})}{\rho}} \tag{13}$$

Where ΔA is differential area, m^2; $k_{\Delta A}$ is differential regulation coefficient; x_5 is spool displacement of direct-acting valve, mm; x_7 is spool displacement of the differential valve, mm; p_{sys} is detected pressure, Mpa; $C_{d-relief}$ is two-stage safety valve flow coefficient; $\rho$is density of hydraulic oil, kg/m^3; p_{sub} is mean value of sub-critical pressure, Mpa.

Given that the gas in the upper chamber of the accumulator and the rodless chamber of the hydraulic cylinder deviates from the ideal polytropic process, a sub-critical correction coefficient λ_{sub}, to modify the gas state equation.

$$p \cdot V^n = p_0 \cdot V_0^n \cdot \left[1 + \lambda_{sub} \cdot \frac{p - p_{sub}}{p_{sub}}\right] \tag{14}$$

Where n is polytropic index of the gas in the subcritical range, 1~1.4; p_0 is initial gas pressure, Mpa; V_0 is initial gas volume, Mpa; p is real-time gas pressure, Mpa。

(2) Equation for the Actual Flow Rate of the Hydraulic Pump

$$q_p = q_{pt} - C_{ip}(p_1 - p_{relief}) - \frac{V_p}{K} \cdot \frac{dp_1}{dt} \tag{15}$$

Where q_{pt} is theoretical flow rate of a pump, m^3/s; C_{ip} is pump leakage coefficient, m^3/(s • Pa) ; p_1 is pump outlet pressure, Mpa; V_p is pump outlet volume, m^3,

(3) Cartridge valve

The cartridge valve provides a bypass for the pump flow, and its outlet flow is influenced by the coupling of the downstream pressure and the unloading pressure of the two-stage valve. The model is as follows:

$$q_{cv} = C_{dcv} \cdot \sqrt{\frac{2(p_1 - p_2)}{\rho}} \tag{16}$$

Where C_{dcv} is cartridge valve flow conductance coefficient.

(4) Accumulator

The mathematical model for the accumulator is established by incorporating the pressure feedback term of the two-stage pressure relief valve and the non-linear gas compression term: Electro-hydraulic hammer return stroke:

Piston equation of motion

$$m_a\ddot{x}_a = p_{up} \cdot A_a - p_2 A_a - F_{fa} - k_{coup} \cdot (p_2 - p_{relief}) \cdot A_a \quad (17)$$

Equation of state for gas adapted to subcritical conditions:

$$p_{up}V_a^n = p_{up0}V_{a0}^n \cdot \left(1 + \lambda_{sub} \cdot \frac{p_2 - p_{sub}}{p_{sub}}\right) \quad (18)$$

Flow coupling equation:

$$A_a\dot{x}_a + q_{cv} = q_v + q_{relief} + \frac{V_2}{K} \cdot \frac{dp_2}{dt} \quad (19)$$

Where m_a is accumulator piston mass, kg; A_a is piston area, m^2; F_{fa} is flow coupling equation, N; k_{coup} is accumulator-two-stage pressure relief valve coupling coefficient; p_{up0} is initial gas pressure, Mpa; V_{a0} is initial gas volume, m^3; p_2 is oil pressure of node 2, Mpa; F_{fa} is total friction resistance of piston, N; q_v is main control valve inlet flow rate, m^3/s, V_2 is volume at node 2, m^3; p_{up} is real-time gas pressure, Mpa.

Striking phase of the electro-hydraulic hammer:

Piston equation of motion

$$m_a\ddot{x}_a = p_2 A_a - p_{up} \cdot A_a - F_{fa} - k_{coup} \cdot (p_{relief} - p_2) \cdot A_a \quad (20)$$

Equation of state for gas adapted to subcritical conditions:

$$p_{up}V_a^n = p_{up0}V_{a0}^n \cdot \left(1 + \lambda_{sub} \cdot \frac{p_2 - p_{sub}}{p_{sub}}\right) \quad (21)$$

Flow coupling equation:

$$q_{p-surp} + A_{hr}\dot{x}_h = A_a\dot{x}_a + q_{relief} + \frac{V_2}{K} \cdot \frac{dp_2}{dt} \quad (22)$$

(4) Main control valve

For the main control valve, a three-position, three-way directional control valve, the equation of motion for the spool during the return stroke is as follows:

$$m_v\ddot{x}_v + c_v\dot{x}_v + k_v x_v = (p_3 - p_{relief}) \cdot A_v - F_{fv} \quad (23)$$

Where m_v is spool mass, kg; x_v is spool displacement, m; p_3 is oil pressure at node 3, Mpa; A_v is oil action area, m^2; $k_v$is spring stiffness, N/s; F_{fv} is the sum of friction, N.

The flow equation of the backhaul process is:

$$q_v = C_{dv}A_v(x_v) \cdot \sqrt{\frac{2(p_3 - p_4)}{\rho}} \quad (24)$$

Where σ_{23} is comprehensive flow coefficient of valve port.

When the reversing valve is in the hammer blow position, the valve core motion equation is:

$$m_v\ddot{x}_v + c_v\dot{x}_v + k_v x_v = (p_t - p_{relief})A_v - F_{fv} \quad (25)$$

Where p_t is tank oil pressure, Mpa; F_{fv} is frictional force, N.

The flow equation of the striking process is:

$$q_{vh} = \sigma_{dv}A_{vh}\sqrt{\frac{2(p_{relief} - p_t)}{\rho}} \quad (26)$$

(5) Fast drain valve

For the purpose of mathematical modeling, the fast drain valve is treated as a functional equivalent of a combination of a check valve, a throttle valve, and a differential piston. In developing the model for its operation in both the return and striking strokes, a key assumption is made that the friction between the floating sleeve and the floating ring is constant.

The kinematic equation of the floating spool during the return stroke is:

$$m_q\ddot{x}_q = p_4 A_{qr} - p_t A_{ql} - F_{fq} \quad (27)$$

Flow equation:

$$q_q \approx 0 \quad (28)$$

Where m_q is the mass of the valve core, kg; x_q is the displacement of the valve core, m;A_{qr} is the end face area of the main control valve spool floating on the right side of the spool, m^2; A_{ql} is the the end face area of the main control valve spool floating on the left side of the spool, m^2; p_4 is oil pressure of node 4, Mpa; F_{fq} is the sum of various frictions, N.

The kinematic equation of the floating spool during the return stroke is:

$$m_q\ddot{x}_q = p_t A_{qr} - p_4 A_{ql} - F'_{fq} \quad (29)$$

Flow equation:

$$q_q = C_{dq}A_q \cdot \sqrt{\frac{2(p_4 - p_t)}{\rho}} \quad (30)$$

Where C_{dq} is quick discharge valve hydraulic conductivity coefficient; F'_{fq} is valve core friction, N; A_q is co-flow area of quick discharge valve port, m^2.

(7) G hydraulic cylinder

Piston work equation of hydraulic cylinder return stroke:

$$m_h\ddot{x}_h = p_4 A_{hr} - p_0 A_{h0} - F_{fh} - G_h \quad (31)$$

Nonlinear state equation of rodless cavity gas:

$$p_0(V_{00} - A_{h0}x_h)^n = p_{00}V_{00}^n \cdot \left[1 + \lambda_{sub} \cdot \frac{p_0 - p_{sub}}{p_{sub}}\right] \quad (32)$$

Backhaul flow equation:

$$q_v = A_{hr}\dot{x}_h + \frac{V_4}{K} \cdot \frac{dp_4}{dt} \quad (33)$$

Where m_h is mass of hydraulic cylinder piston and hammer head, kg; $x_h$is Hydraulic cylinder piston displacement, m; A_{hr} is piston area of rod cavity, m^2; A_{h0} is the displacement of the hydraulic cylinder piston, m^2; V_4 is hydraulic cylinder rodless cavity volume, m^3; V_{00} isInitial volume of upper cavity of hydraulic cylinder, m^3; p_{00} is initial pressure of upper chamber

of hydraulic cylinder, Mpa.

The motion equation of piston during striking stroke:

$$m_h\ddot{x}_h = p_0A_{h0} + G_h - p_4A_{hr} - F'_{fh} - D_{lcf}\cdot\sigma_{fluc}(p_4)\cdot A_{hr} \quad (34)$$

Flow equation during strike:

$$p_0(V_{00} - A_{h0}x_h)^n = p_{00}V_{00}^n\cdot\left[1+\lambda_{sub}\cdot\frac{p_0-p_{sub}}{p_{sub}}\right] \quad (35)$$

Where F'_{fh} is friction force during striking stroke, N.

$$A_{hr}\dot{x}_h = q_q + q_{relief} + \frac{V_4}{K}\cdot\frac{dp_4}{dt} \quad (36)$$

D_{lcf} is low cycle fatigue damage coefficient; $\sigma_{fluc}(p_4) = k_\sigma(p_4 - p_{sub})^2$ is stress pulsation induced by sub-critical pressure; F'_{fh} is hydraulic ram friction force, N.

According to the node constraint topology conditions and each sub-element and mathematical model, the mathematical model of the hydraulic system of the electro-hydraulic hammer striking process and the return process can be established:

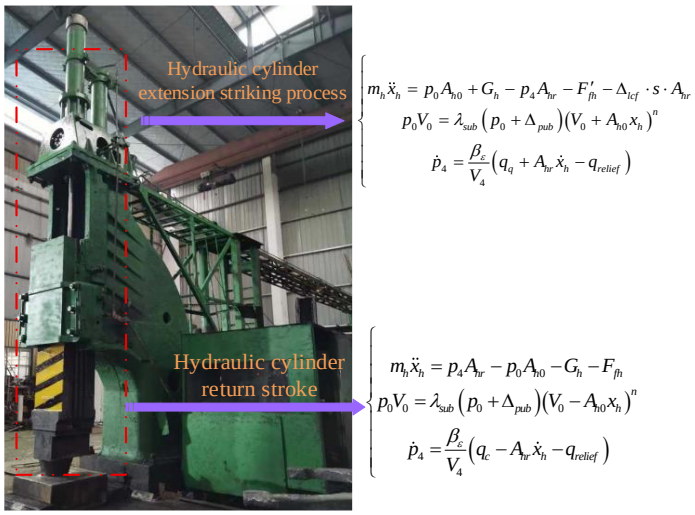

$$\begin{cases} m_h\ddot{x}_h = p_0A_{h0} + G_h - p_4A_{hr} - F'_{fh} - \Delta_{lcf}\cdot s\cdot A_{hr} \\ p_0V_0 = \lambda_{sub}\left(p_0+\Delta_{pub}\right)\left(V_0 + A_{h0}x_h\right)^n \\ \dot{p}_4 = \frac{\beta_e}{V_4}\left(q_q + A_{hr}\dot{x}_h - q_{relief}\right) \end{cases}$$

$$\begin{cases} m_h\ddot{x}_h = p_4A_{hr} - p_0A_{h0} - G_h - F_{fh} \\ p_0V_0 = \lambda_{sub}\left(p_0+\Delta_{pub}\right)\left(V_0 - A_{h0}x_h\right)^n \\ \dot{p}_4 = \frac{\beta_e}{V_4}\left(q_c - A_{hr}\dot{x}_h - q_{relief}\right) \end{cases}$$

Figure 9. Electro-hydraulic hammer strike and return process model.

The mathematical model for the electro-hydraulic hammer delineates two distinct operational phases. For the return stroke, the model simulates the upward movement of the piston driven by high-pressure oil. This phase encompasses the pressure-fluctuation suppression during accumulator discharge, the reversal of the main control valve to the return position, the closure of the fast drain valve, and the standby condition of the secondary pressure-regulating valve. Conversely, for the strike stroke, the model simulates the hammer's free-fall stage [17]. This includes the instantaneous pressure relief within the lower chamber, the counter-pressure from the gas in the upper chamber, and the transient unloading behavior of the safety valve in response to the sudden impact load induced by the opening of the fast drain valve.

3.2. Electro-hydraulic hammer hydraulic system simulation analysis

To validate the proposed Dual-stage relief valve's capability to suppress Low-Cycle Fatigue (LCF) at the system level, a comprehensive dynamic model was developed [18]. This model uniquely embeds the valve's hierarchical response mechanism for sub-critical transients (35–40 MPa) and adaptive gas compression terms, establishing a direct link between pressure regulation and fatigue suppression. A high-fidelity co-simulation of the entire electro-hydraulic hammer system was then constructed on the AMESim/Simulink platform using parameters from Table 4, specifically to replicate the transient hydraulic shocks responsible for LCF.

Table 4. Main parameters of electro-hydraulic hammer hydraulic system.

Name	Symbol	Value	Unit
Accumulator piston mass	m_a	19	kg
Accumulator piston area	A_a	2.6×10^{-2}	m^2
Total friction of accumulator piston	F_{fa}	1000	N
Initial volume of accumulator oil chamber	V_{a0}	2.5	m^3
Liquid action area of main control valve	A_v	3.22×10^{-3}	m^2
Oil pump flow Conductance	C_{ip}	6×10^{-11}	$m^3/(s\cdot Pa)$
Cartridge valve hydraulic guide	C_{dcv}	8.77×10^{-9}	$m^3/(s\cdot Pa)$
The total flow coefficient of the main control valve port	C_{dv}	2.09×10^{-6}	
Quick release valve (check valve) flow conductance	C_{dp1}	6.78×10^{-6}	$m^3/(s\cdot Pa)$
Quick release valve (throttling speed control valve) flow conductance	C_{dp2}	8.32×10^{-9}	$m^3/(s\cdot Pa)$
Sum of friction of main control valve	F_{fv}	0	N
Sum of friction of quick release valve	F_{fq}	0	N
Total friction of hydraulic cylinder	F_{fh}	12000	N
Accumulator piston area	A_{ae}	0.1521	m^2
Hydraulic cylinder rod cavity area	A_{hr}	1.4	m^2
Hydraulic cylinder rodless cavity area	A_{h0}	2.5	m^2
Mass of hydraulic cylinder piston and hammer head	m_h	5500	kg
Hydraulic cylinder rodless cavity air pressure	P_{00}	3	Mpa
Initial gas volume of hydraulic cylinder	V_{00}	0.15	m^3
the bulk modulus of oil	K	700	Mpa
Transient dynamic coefficient	φ	0	
viscous damping coefficient	c	0	N • s/m
Mass of quick release valve spool	m_q	2.2	kg

To validate the proposed ΔA-driven valve's efficacy in

mitigating Low-Cycle Fatigue (LCF), a high-fidelity co-simulation model of the return process was constructed on the AMESim/Simulink platform. The model centers on the sub-model of the proposed dual-stage pressure-regulating valve, which embeds its hierarchical response mechanism for sub-critical transients [19]. As depicted in Figure 10, this core sub-model is integrated into a comprehensive system framework that includes the dynamics of the hydraulic pump, accumulator, main control valve, and hydraulic cylinder. This holistic approach creates a realistic environment to simulate the specific pressure fluctuations responsible for LCF and rigorously test the valve's proactive suppression capabilities.

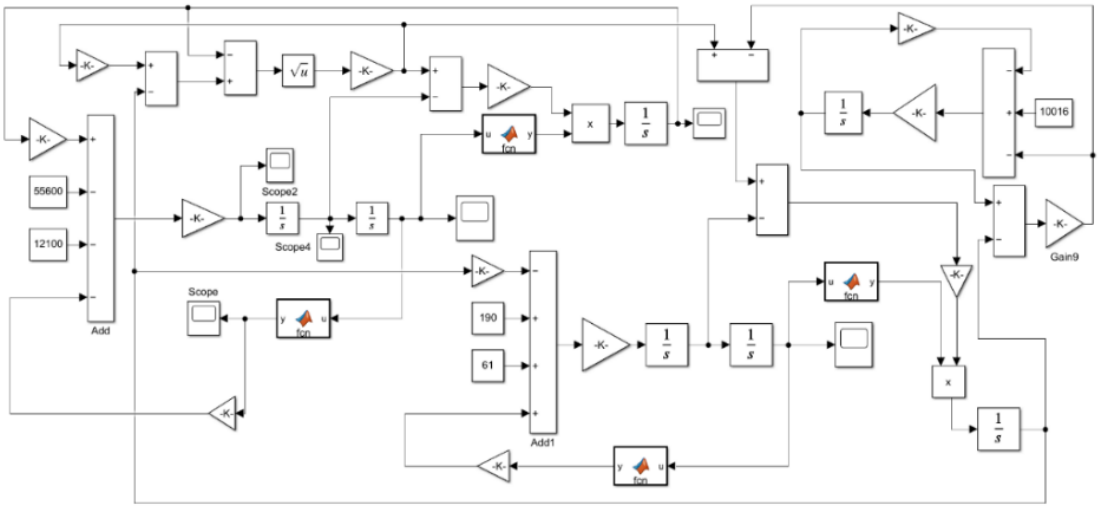

Figure 10. Simulation model of electro-hydraulic hammer return process.

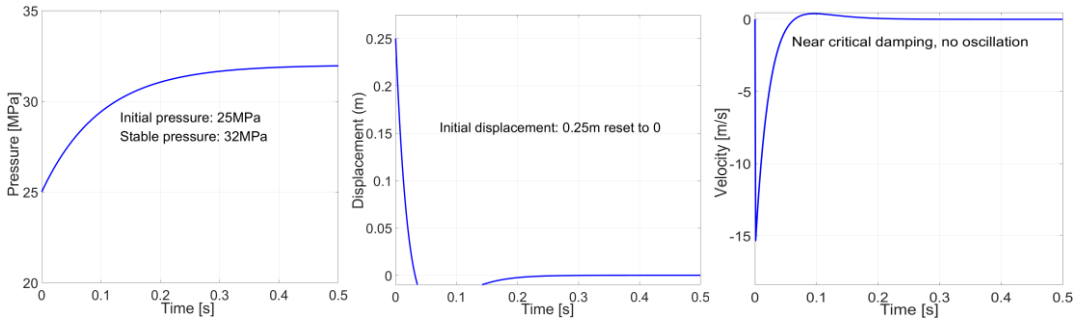

(a) (b) (c)

Figure 11. Simulation curve of electro-hydraulic hammer return process.

To evaluate the impact resistance and dynamic stability of the electro-hydraulic hammer system equipped with the proposed Dual-stage relief valve, co-simulations of the return and strike processes were conducted under transient hydraulic shock loads [20,21].

Figure 11 illustrates the system's dynamic response during the return stroke, specifically demonstrating the valve's core function. As shown in Figure 11(a), the Dual-stage relief valve proactively regulates pressure, clamping it at approximately 32 MPa. This pressure level is deliberately set below the sub-critical range (35–40 MPa)—the fatigue-prone zone where conventional valves exhibit a "dead zone"—thus preventing the system from entering the damaging pressure interval. By doing so, the valve eliminates repetitive hydraulic shocks that are the primary cause of low-cycle fatigue (LCF). The rapid 0.02 s response time is critical to this preemptive regulation. Consequently, the piston displacement and velocity profiles in Figures 11(b) and 11(c) are smooth and stable, laying a solid foundation for the operational stability of the system and the longevity of its components.

To further validate the ΔA-driven valve's capability to suppress sub-critical transients (the root cause of LCF), a high-fidelity simulation of the strike process was developed. This model integrates the dynamics of all core system components and embeds the proposed valve's sub-model. The simulation first reproduces a typical striking cycle, which inherently generates recurring sub-critical pressure fluctuations (35–40 MPa). Subsequently, an instantaneous 40 MPa impact load—

representing the upper limit of the sub-critical range—is applied at 0.1 s to rigorously test the valve's performance. This test verifies the valve's ability to precisely regulate pressures within the target sub-critical range while withstanding high-energy shocks. The system's pressure, displacement, and velocity responses were monitored to assess the valve's efficacy in eliminating fatigue-inducing pressure spikes and ensuring operational stability. The simulation results are presented in Figure 12.

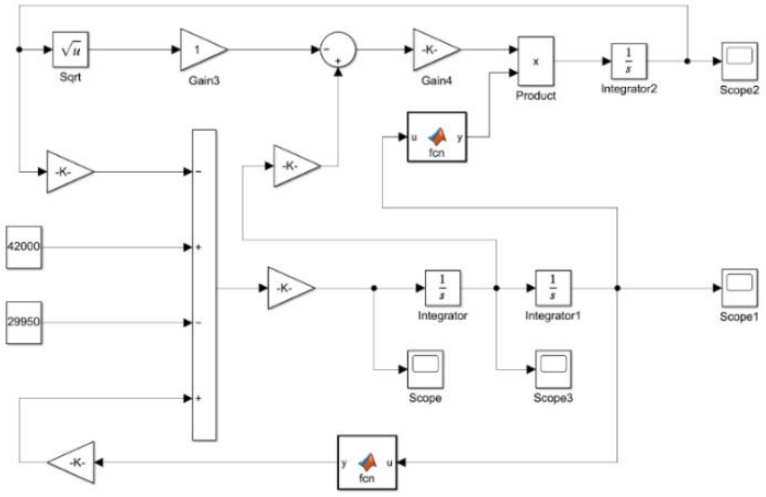

Figure 12. Simulation model of electro-hydraulic hammer strike process.

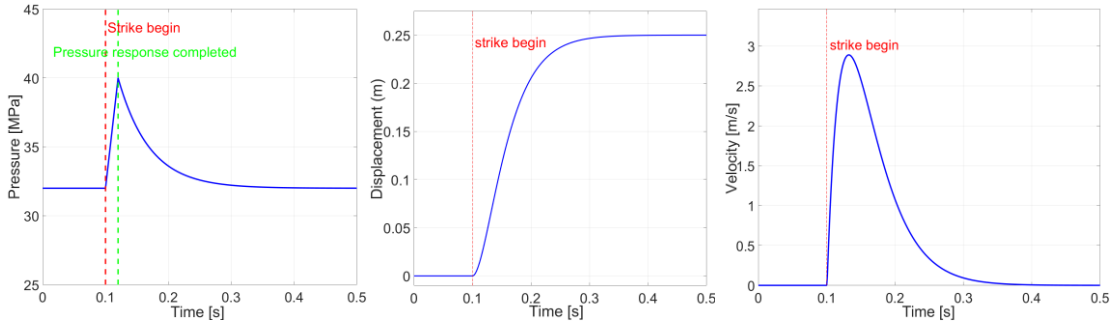

(a) (b) (c)

Figure 13. Simulation curve of electro-hydraulic hammer strike process.

Figure 13 illustrates the system's dynamic response during striking, specifically validating the valve's role in mitigating LCF. As shown in Figure 13(a), when a 40 MPa impact load—representing the upper limit of the sub-critical pressure range (35–40 MPa) is applied at 0.1 s, the valve responds immediately, completing the unloading process within 0.02 s. This rapid response—consistent with its designed dynamic performance—is critical for proactively suppressing pressure spikes, which are the primary driver of the cyclic loading that induces LCF. The smooth and oscillation-damped profiles of piston displacement and velocity in Figures 13(b) and 13(c) are not merely indicators of general stability; they are direct evidence of the valve's success in attenuating fatigue-inducing pressure transients. This confirms that the valve fundamentally mitigates the driving mechanism of LCF while ensuring the integrity of the striking action without compromising the hammer's operational performance.

4. Multi-scale modeling and experimental validation of LCF suppression in electro-hydraulic systems

This study establishes a direct correlation among the dynamic performance, cyclic stress evolution, and service life of components to comprehensively validate the low-cycle fatigue (LCF) suppression effect of a dual-stage safety valve at the electro-hydraulic hammer system level [22,23]. Through mechanism analysis, theoretical life prediction, and system-level experimental validation, the valve's capability to eliminate LCF induced by subcritical pressure is quantitatively demonstrated.

4.1. Pressure-stress analysis of fatigue damage in the dual-stage safety valve

The LCF failure of the electro-hydraulic hammer components is caused by repeated subcritical pressure fluctuations (35-40 MPa) during the forging cycle. Traditional safety valves exhibit a 'dead zone' within this pressure range, unable to attenuate fluctuations, which translates into cyclic stress loads on structural components. After thousands of cycles, this cyclic stress can lead to crack initiation and propagation, ultimately resulting in premature failure.

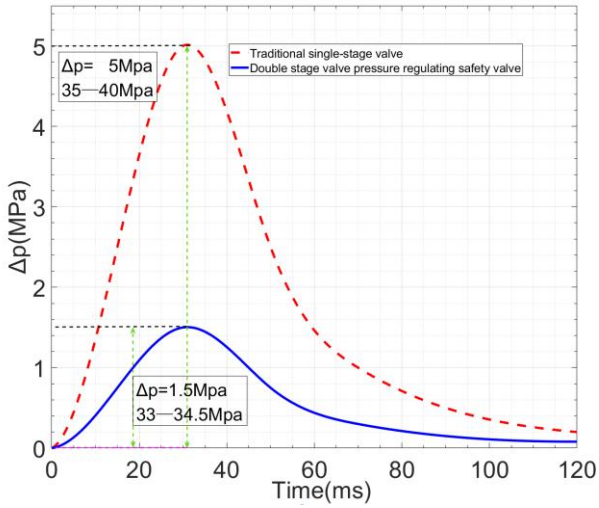

Figure 14. Comparison curves of pressure amplitudes for two types of valves.

The two-stage valve solves this fundamental problem through its graded response mechanism: the differential stage (ΔA=796.24×10⁻⁶ m²) actively regulates subcritical pressure (35-40MPa), while the direct acting valve mainly deals with catastrophic surge (>40 MPa). This dynamic adjustment directly reduces the pressure amplitude (Δp) of subcritical fluctuations from the traditional valve's 5 MPa (35-40 MPa) to the designed 1.5 MPa (33-34.5 MPa), as shown in Figure 14.

According to the thin-walled cylinder stress model:

$$\Delta\sigma = \frac{p_d}{2\delta} \cdot K_t \tag{37}$$

The secondary valve significantly lowers low-cycle fatigue (LCF) risk by attenuating cyclic stress [24]. Leveraging the linear $\Delta\sigma$-Δp relationship, a 70% cut in pressure amplitude directly diminishes the cyclic stress at its source. Experiments confirm a sharp decrease in stress amplitude at a critical hydraulic cylinder port, from 108.1 MPa (conventional valve) to 43.2 MPa. This substantial stress reduction interrupts the fatigue damage mechanism, enabling effective system-level LCF mitigation.

4.2. Life prediction model considering subcritical amplitude pressure and stress concentration

During the forging process of an electro-hydraulic hammer, subcritical pressure fluctuations are affected by the forging material, impact energy, and equipment wear, exhibiting random amplitude characteristics (fluctuation amplitude of 3-5 MPa, frequency of 10-20 Hz, and random distribution of peak values). The traditional Miner theory assumes linear superposition of damage, which cannot reflect the coupling effect of "high amplitude load accelerating low amplitude load damage" under variable amplitude load. Therefore, the modified Miner theory is adopted:

Assuming that the damage accumulates independently in each cycle, when the total damage reaches 1, the component fails:

$$D = \sum_{i=1}^{n} \frac{n_i}{N_{f,i}} \cdot \alpha_i \tag{38}$$

Where: n_i is the number of cycles at the 'i'-th load level. $N_{f,i}$ is the fatigue life (in cycles) corresponding to the 'i'-th load level. α_i is the load sequence correction factor, defined as the damage amplification factor for the 'i'-th load level.

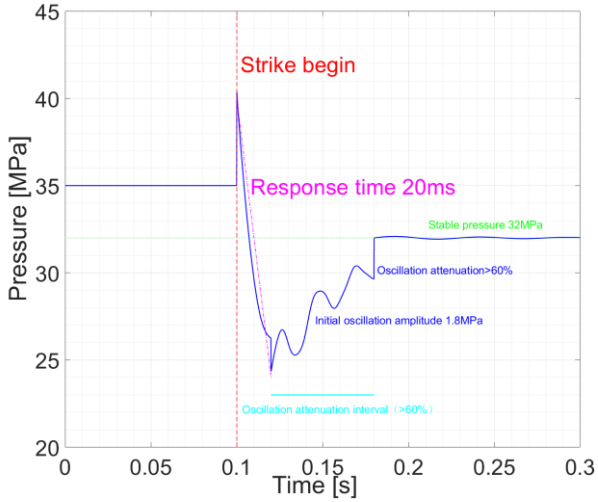

Figure 15. Measurement curve of amplitude pressure of the hydraulic cylinder.

Statistical fitting of the measured variable amplitude pressure data from the electro-hydraulic hammer (Figure 15) yields the following:

$$\alpha_i = 1.02\, exp\left(0.1\frac{\Delta p_i}{\overline{\Delta p}}\right) \tag{39}$$

Where: Δp_i is the fluctuation amplitude at the 'i'-th level,

the high amplitude load Δp_i=4 MPa is the average fluctuation amplitude; Δp_i>4 Mpa corresponds to α_i>1, quantifying its accelerating effect on subsequent damage.

The relationship between plastic strain amplitude and fatigue life was obtained by using Goodman to correct the influence of average stress：

$$\Delta\varepsilon_{total} = \Delta\varepsilon_e + \Delta\varepsilon_p = \frac{\Delta\sigma}{E} + 2\varepsilon_f'(2N_f)^c \quad (40)$$

Where: $\Delta\varepsilon_{total}$ represents the total strain amplitude; $\Delta\varepsilon_e$ represents the amplitude of elastic strain; $\Delta\sigma$ represents the stress amplitude, which is converted from pressure fluctuations, Mpa； E is the elastic modulus of the material, Mpa; ε_f' represents the fatigue ductility coefficient, ε_f'=0.23; c is the fatigue ductility index; N_f is the fatigue life corresponding to a single cycle, times.

The core components such as the hydraulic cylinder body and valve core undergo structural mutations, resulting in local stress concentration (concentration factor K_t=1.2~1.5). The traditional uniform stress model cannot explain the failure law of "local high stress areas preferentially initiate cracks". Introducing stress gradient factor β to correct local stress calculation:

$$\Delta\sigma_{local} = \Delta\sigma \cdot K_t \cdot \beta \quad (41)$$

Where: $\Delta\sigma$ represents the amplitude of the equilibrium cyclic stress, Mpa； β is the stress gradient factor, the ratio of the local maximum stress to the average stress, $K_t$is the local stress concentration factor, and K_t=1.3.

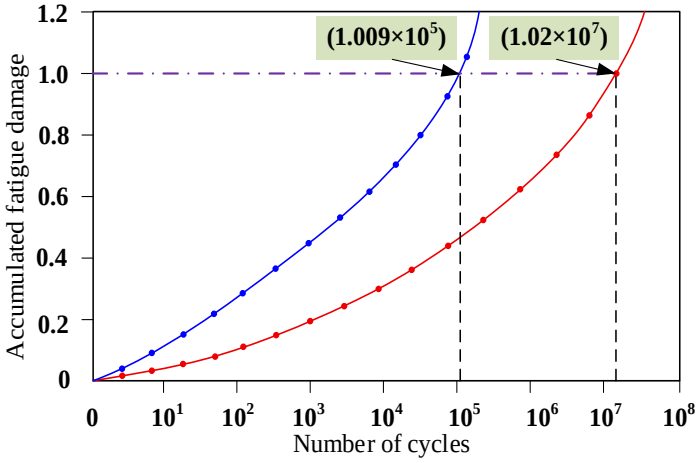

Figure 16. Comparison of cumulative damage curve simulation.

Therefore, the core equation for refined LCF life prediction is revised to:

$$\Delta\varepsilon_t = \frac{\Delta\sigma_{local}}{E} + \varepsilon_f'(2N_f)^c \quad (42)$$

$$D = \sum_{i=1}^{k} \frac{n_i}{N_{fi}} \cdot \alpha_i \quad (43)$$

Where: c is the fatigue ductility index of 30CrMo steel, c =-0.65.

4.3. Experimental verification of the LCF suppression efficiency of the two-stage pressure regulating safety valve

To quantitatively validate the LCF mitigation advantage of a dual-stage valve over a conventional one, an accelerated fatigue test was conducted using 30CrMo steel specimens (±0.1 mm tolerance) on an MTS 810 testing machine. The dual-stage valve effectively regulates sub-critical pressure fluctuations in the 35–40 MPa range, reducing the pressure amplitude from 5 MPa to 1.5 MPa and thus suppressing LCF damage, representing a 70% amplitude reduction. A multi-sensor system, including 1 kHz strain gauges, a 0.1 mm resolution ultrasonic detector, and a ±0.5°C infrared thermometer, was employed to monitor strain response, crack initiation/propagation, and thermal effects, respectively, for comprehensive damage characterization and model calibration.

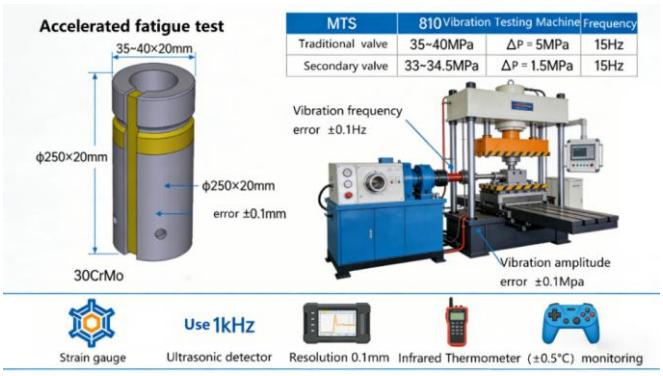

Figure 17. Accelerated fatigue experiment of electro-hydraulic hammer system.

An NI cDAQ-9178 system facilitated synchronized multi-device data acquisition (±1 μs timestamp accuracy). Real-time data at 1 kHz included pressure peaks/valleys, strain (converted to stress via Hooke's law and corrected with a 1.3 stress gradient factor), and specimen temperature. Intermittently, an ultrasonic detector logged crack length and cycles to initiation, while checks were made on strain gauge adhesion and load stability. All TDMS data, tagged by cycle count, were converted to CSV for post-processing. This process calculated cumulative damage (modified Miner's rule), stress attenuation, and life

parameters to generate characteristic curves with a relative error ⩽ 5% (Figure 18).

The LCF mitigation performance of the ΔA-driven dual-stage valve is demonstrated by comparing cumulative damage evolution (Fig. 18). Under the conventional valve, damage increases linearly and rapidly, reaching failure (D=1) at 9.6×10^4 cycles (12.5 h), confirming accelerated failure from subcritical pressure fluctuations. In contrast, the dual-stage valve drastically slows the damage rate; the service life of 9.8×10^6 cycles (1283.3 h) is a theoretical prediction derived from the accelerated fatigue experimental stress data (including the measured stress amplitude attenuation from 108.1 MPa to 43.2 MPa and the modified Miner's damage accumulation model). The accelerated fatigue test physically verified the damage accumulation trend and stress attenuation effect, and the theoretical life was extrapolated from the experimentally calibrated damage model with a relative error of only 3.92%. This improvement is attributed to its staged response mechanism: by using ΔA to reduce the pressure fluctuation amplitude from 5 MPa to 1.5 MPa, the cyclic stress amplitude is attenuated from 108.1 MPa to 43.2 MPa, effectively breaking the pathway to fatigue damage.

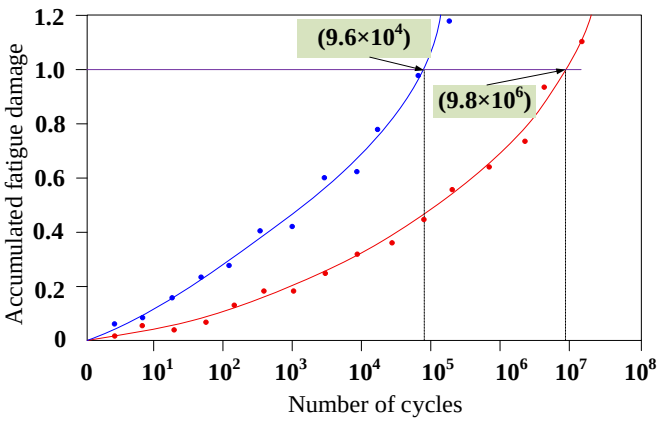

Figure 18. Experimental comparison of cumulative damage curves.

Table 5. Experimental damage life comparison.

Working condition type	Theoretical predicting lifespan	Physically tested accelerated fatigue lifespan	relative error	Crack initiation time (h)
Single stage valve	1.009×10^5	9.6×10^4	4.86%	12.5
Secondary safety valve	1.02×10^7	9.8×10^6	3.92%	1283.3

The experimental curves' reliability is confirmed by multi-sensor data, with stress attenuation matching damage accumulation rates and crack initiation aligning with curve inflection points (relative error < 5%). The results validate the ΔA-driven design's core advantage: active suppression of pressure transients drastically reduces the damage accumulation rate, boosting component life by nearly two orders of magnitude and offering direct experimental proof for system reliability optimization. Main error sources include temperature variations (±2°C) and material variability (±3% E-modulus), but overall accuracy remains within engineering limits (<5%). Crucially, the crack initiation time was extended by a factor of 102.7, consistent with the life extension trend.

5. Conclusion

This study addresses the critical issue of low-cycle fatigue (LCF) in electro-hydraulic hammers caused by sub-critical pressure transients (35–40 MPa), a problem unresolved by conventional relief valves due to their inherent response dead zone. A novel Dual-stage relief valve is proposed, integrating direct-acting and pilot-operated differential mechanisms to decouple high- and low-pressure regulation.

1) The hierarchical response mechanism based on the fixed structural parameter ΔA eliminates the sub-critical pressure dead zone, realizing proactive regulation of 35–40 MPa fluctuations while handling catastrophic surges (>40 MPa).
2) Experimental and simulation results confirm exceptional dynamic performance: 20 ms response time (40% improvement), >60% oscillation attenuation, and reduction of pressure fluctuation amplitude from 5 MPa to 1.5 MPa, cutting cyclic stress from 108.1 MPa to 43.2 MPa.
3) Based on experimental stress amplitude data and the modified Miner's fatigue life prediction model, the valve is predicted to extend the component service life by nearly two orders of magnitude (from the experimentally verified 9.6×10^4 cycles of the single-stage valve to 9.8×10^6 cycles), and stabilizes system pressure at 32 MPa, shifting hydraulic system reliability from passive protection to proactive management.

This design enriches relief valve theory and provides

a practical solution for high-reliability hydraulic systems in heavy forging and other high-load industries. Future research will focus on adaptive ΔA control for variable conditions and performance optimization under extreme environments.

Acknowledgment

This research was funded by Jilin University of Chemical Technology Research Funding & Jilin Provincial Department of Education of China. Project Number: JJKH20240306KJ.

References

1. Ye Z, Li W, Xu Y, Jin Z, Qian J. Effects of adjusting ring and spring stiffness on fluid dynamics of steam spring-loaded safety valve. Nuclear Engineering and Technology 2025; 57(5): 103338. https://doi.org/10.1016/j.net.2024.11.040.
2. Xu B, Ding R, Zhang J, Yang G, Li J. Modeling and dynamic characteristics analysis on a three-stage fast-response and large-flow directional valve. Energy Conversion and Management 2014; 79: 187–199. https://doi.org/10.1016/j.enconman.2013.12.013.
3. Dai K, Xie F, Gao Q, Zhang D, Ding E, Guo X. Theoretical and experimental research on the pressure response characteristics of cartridge electromagnetic relief valve. International Journal of Structural Integrity 2018; 9(1): 65–75. https://doi.org/10.1108/IJSI-03-2017-0020.
4. Ma A, Yuan W, Wang N, Chen H, Li Z. Multiobjective optimization design of a two-stage high-speed on/off valve based on the electric eel foraging optimization algorithm. IEEE Transactions on Industrial Electronics 2025; 72(5): 5210–5220. https://doi.org/10.1109/TIE.2024.3476962.
5. Xu W, Wang Q, Wu D, Li Q. Simulation and design improvement of a low noise control valve in autonomous underwater vehicles. Applied Acoustics 2019; 146: 23–30. https://doi.org/10.1016/j.apacoust.2018.10.019.
6. Barbaryan T, Hoseinzadeh S, Heyns P S, Nematollahi M. Developing a low-fluid pressure safety valve design through a numerical analysis approach. International Journal of Numerical Methods for Heat & Fluid Flow 2019; 30(3): 1427–1440. https://doi.org/10.1108/HFF-06-2019-0508.
7. Zang J, Yao H, Zhang F, Liu X, Wang Y. Dynamic characteristics analysis of pilot valves with different inlet diameters installed on the main steam valve set. Case Studies in Thermal Engineering 2022; 34: 102004. https://doi.org/10.1016/j.csite.2022.102004.
8. Yang L, Wang Z, Dempster W, Yuan X, Peng B. Experiments and transient simulation on spring-loaded pressure relief valve under high temperature and high pressure steam conditions. Journal of Loss Prevention in the Process Industries 2017; 45: 133–146. https://doi.org/10.1016/j.jlp.2016.12.003.
9. Zong C, Shi M, Li Q, Zhao Y, Zhang H. Design optimization of a nuclear main steam safety valve based on an E-AHF ensemble surrogate model. Nuclear Engineering and Technology 2022; 54(11): 4181–4194. https://doi.org/10.1016/j.net.2022.06.019.
10. Qian J, Hou C, Mu J, Chen X, Wu Y. Valve core shapes analysis on flux through control valves in nuclear power plants. Nuclear Engineering and Technology 2020; 52(10): 2173–2182. https://doi.org/10.1016/j.net.2020.03.008.
11. Bossard J, Reich A, DiMeo A. Dynamic analysis of a high-pressure relief valve during opening. Journal of Pressure Vessel Technology 2021; 143(1): 011701. https://doi.org/10.1115/1.4047865.
12. Kádár F, Stépán G. Nonlinear dynamics and safety aspects of pressure relief valves. Nonlinear Dynamics 2023; 111(13): 12017–12032. https://doi.org/10.1007/s11071-023-08484-w.
13. Li T, Zhang Y, Liang Y, Wang S, Liu H. Multiobjective optimization research on the response time of a pneumatic pilot-operated high speed on/off valve. International Journal of Applied Electromagnetics and Mechanics 2020; 65(1): 109–127. https://doi.org/10.3233/JAE-190074.
14. Lisowski E, Filo G. Analysis of a proportional control valve flow coefficient with the usage of a CFD method. Flow Measurement and Instrumentation 2017; 53: 269–278. https://doi.org/10.1016/j.flowmeasinst.2016.12.009.
15. Ren H, Zhang D, Gong S, Wu C, Yang F. Dynamic impact experiment and response characteristics analysis for 1:2 reduced-scale model of oil production equipment. International Journal of Mining Science and Technology 2021; 31(3): 347–356. https://doi.org/10.1016/j.ijmst.2021.03.004.
16. Hu M. Design and development of a high-precision automatic safety valve testing system. Advances in Mechanical Engineering 2020; 12(4): 1–15. https://doi.org/10.1177/1687814020914733.
17. Zhang H, Liao Y, Tao Z, Chen L, Wu J. Modeling and dynamic characteristics of a novel high-pressure and large-flow water hydraulic

proportional valve. Machines 2022; 10(1): 37. https://doi.org/10.3390/machines10010037.
18. Lyu F, Cao C, Zhao D, Li C, Su J, Zhao X, Jia X. Vibration characteristics analysis of high-pressure long-distance dense paste pipeline transporting with hydraulic active check valve. Alexandria Engineering Journal 2023; 71: 669–677. https://doi.org/10.1016/j.aej.2023.03.086.
19. Abdallah H K, Peng J, Li S. Analysis of pressure oscillation and structural parameters on the performance of deflector jet servo valve. Alexandria Engineering Journal 2023; 63: 675–692. https://doi.org/10.1016/j.aej.2022.11.021.
20. Zhang Y, Xia Y. Analysis and optimization of the pilot stage of jet pipe servo valve. Alexandria Engineering Journal 2022; 61(1): 41–50. https://doi.org/10.1016/j.aej.2021.04.087.
21. Kang J, Yuan Z, Sadiq M T. Numerical simulation and experimental research on flow force and pressure stability in a nozzle-flapper servo valve. Processes 2020; 8(11): 1404. https://doi.org/10.3390/pr8111404.
22. Li C, Yin Y, Wang M, Wang F. Influence of high temperature on couples matching and characteristics of jet pipe electrohydraulic servo valve. Journal of Mechanical Engineering 2018; 54(20): 251–261. https://doi.org/10.3901/JME.2018.20.251.
23. Yuan G, Zhang X, Chen B, Tu S, Zhang C. Low-cycle fatigue life prediction of a polycrystalline nickel-base superalloy using crystal plasticity modelling approach. Journal of Materials Science & Technology 2020; 38: 28–38. https://doi.org/10.1016/j.jmst.2019.05.072.
24. Yuan Y, Zhou J, Cui Q, Yang Y, Fei X, Wang Y. Multi-physics coupling analysis and fatigue prediction modeling for wind turbine gear transmission systems. Engineering Failure Analysis 2026; 186(A): 110489. https://doi.org/10.1016/j.engfailanal.2025.110489.